Computational simulation of subatomic-resolution AFM and STM images for graphene/hexagonal boron nitride heterostructures with intercalated defects

Junsu Lee, Minjung Kim, James R. Chelikowsky, and Gunn Kim

Phys. Rev. B **94**, 035447 — Published 29 July 2016

DOI: 10.1103/PhysRevB.94.035447

Computational simulation of subatomic-resolution AFM and STM images for graphene/hexagonal boron nitride heterostructures with intercalated defects

Junsu Lee,[1] Minjung Kim,[2,3] James R. Chelikowsky,[2,4] and Gunn Kim[1,5,*]

[1]*Department of Physics & Astronomy,*
Sejong University, Seoul 143-747, Korea
[2]*Department of Chemical Engineering,*
The University of Texas at Austin, Austin, Texas 78712, USA
[3]*Department of Applied Physics, Yale University,*
New Haven, Connecticut 06520, USA
[4]*Department of Physics and Center for Computational Materials,*
Institute for Computational Engineering and Sciences,
The University of Texas at Austin, Austin, Texas 78712, USA
[5]*Graphene Research Institute, Sejong University, Seoul 143-747, Korea*

Abstract

Using *ab initio* density functional calculations, we predict subatomic-resolution atomic force microscopy (AFM) and scanning tunneling microscopy (STM) images of vertical heterostructures of graphene/hexagonal boron nitride (h-BN) with an intercalated metal atom (Li, K, Cr, Mn, Co, or Cu), and study the effects of the extrinsic metal defect on the interfacial coupling. We find that the structural deformation of the graphene/h-BN layer caused by the metal defect strongly affects the AFM images, whereas orbital hybridization between the metal defect and the graphene/h-BN layer characterizes the STM images.

PACS numbers: 81.05.ue, 73.22.Pr, 73.20.Hb

---

[*] The author to whom correspondence should be addressed: gunnkim@sejong.ac.kr

I. INTRODUCTION

Considerable progress has been made in the fabrication and investigation of the vertical heterostructures comprising graphene and other two-dimensional atomic crystals.[1–3] Among various two-dimensional atomic crystals, hexagonal boron nitride (h-BN) monolayer is a promising analogue of graphene for the production of heterostructures exhibiting remarkable physical properties. Through mechanical cleavage, monolayer h-BN can be isolated from its bulk counterpart,[4–6] which is a III-V compound possessing an optical band gap of $\sim$6 eV.[7] As graphene on h-BN has significantly higher carrier mobility[6] than graphene on silicon oxide owing to h-BN's lack of surface dangling bonds, small roughness, and slight lattice mismatch[8] with graphene, few-layer h-BN film has been identified as an effective insulating substrate for graphene-based devices.

Chemical vapor deposition (CVD) is typically used to grow large-area h-BN sheets.[9, 10] Recently, direct growth of a graphene monolayer on a CVD-grown h-BN film was achieved,[11] which yielded superior electronic properties than samples composed of graphene transferred to an h-BN film. Although van der Waals (vdW) interaction itself may be too weak to result in strong coupling at the graphene/h-BN interface, the electronic coupling at the interface could be enhanced as a result of the interfacial contamination from the adsorbates.[1]

In order to understand the structural and electronic properties of graphene nanostructures, atomic force microscopy (AFM) and scanning tunneling microscopy (STM) have been widely used. AFM is a powerful tool for the measurement of various types of forces acting between the AFM tip and the surface.[12, 13] STM, on the other hand, is useful for obtaining information on the local electronic structure of a surface.[14–16] One advantage of AFM over STM is that it facilitates a broader choice of surfaces, as the conducting properties are not required in this procedure. However, an analysis of STM images is aided by a simple theoretical framework wherein one can analyze the convolution of the geometric and electronic structures of a surface or specimen residing on a substrate.

Subatomic-resolution AFM images are usually obtained, using a noncontact frequency-modulation mode in an ultrahigh vacuum environment. Under the conditions, the typical tip-surface distance is a few angstroms,[38] and the short-range forces can lead to improved spatial resolution for the sample images. Further, recent refinements to high-resolution

AFM, which exploit tip apex modification achieved by collecting adatoms or small inorganic molecules,[18, 20–22] have yielded remarkable imaging capabilities in which detailed structural information can be obtained.[39–41]

In the present study, we carry out the *ab initio* calculations of subatomic-resolution AFM and STM images of a graphene/h-BN heterostructure containing an extrinsic defect such as an intercalated metal atom positioned between the graphene and the h-BN sheets. We focus only on the intrinsic properties of each graphene/h-BN heterostructure with the inserted metal impurity. Our simulations reveal that the AFM images are affected by structural deformation of the graphene/h-BN layer owing to the presence of the metal defect, while the STM images show orbital hybridization between the graphene/h-BN layer and the defect. In addition, the findings of this study show that AFM and STM have potential application for distinguishing the types of intercalated impurity atoms in graphene/h-BN heterostructures.

II. COMPUTATIONAL DETAILS

AFM images were obtained by employing the virtual tip (VT) method suggested by Chan *et al.* [25] The traditional method of simulating AFM images is to calculate the forces at each tip position along the three-dimensional trajectory of the tip, using an appropriate tip model. However, there are two major difficulties associated with this approach: (i) The number of simulations required to simulate a full AFM image is extremely large, (ii) The morphology of the AFM tip is unknown. We avoid these problems in our study. Within VT, the interaction between the tip and the sample $F_{ts}(r)$ is defined by the static polarizability of the tip α, such that

$$F_{ts}(r) \approx -\alpha \nabla (|\nabla V_{ts}(r)|)^2 \tag{1}$$

where V_{ts} is the summation of the Hartree and ionic potentials of the sample surface. As α is a constant, no specific model for the tip is required; this significantly reduces the simulation complexity and the computational load. Details of the VT method are found in Refs. 25 and 26. This AFM simulation method has been applied to various surface structures and molecules including an Si(111)–(7×7) surface [25], a GaAs(110) surface [26], and polycyclic aromatic hydrocarbon molecules [27], and the simulated AFM images have in general shown good agreement with the experimental results.

We used real-space DFT package PARSEC [28, 29] to produce the AFM images. The

Kohn–Sham equation in PARSEC is solved on a uniformly spaced grid using pseudopotentials. We apply high-order finite differences to solve for the kinetic energy operator. The convergence is determined by a single parameter, *i.e.*, the grid spacing, which was chosen to be 0.3 a.u. (1 a.u.= 0.5292 Å) for the AFM simulations. Our pseudopotentials were generated by the Troullier–Martins recipe [30]. The Ceperly–Alder [31] local density approximation was used for the exchange-correction functional. The simulation cell was chosen to have dimensions of 12.9×14.9×31.8 $Å^3$, and the k points were sampled at the Γ point only, which is a valid approximation for a supercell of this size.

In order to simulate STM images of graphene/h-BN heterostructures, each containing an intercalated metal atom, we employed the vdW-corrected density functional theory (DFT) calculations of the Vienna ab-initio simulation package (VASP).[32] The STM images were obtained, using the Tersoff–Hamann scheme,[23] which integrates the partial charge densities in a given energy window.

To examine the Coulomb interaction and/or the orbital hybridization of the intercalated atom, we introduced various metal atoms (Li, K, Cr, Mn, Co, and Cu). The details regarding the choice of metal atom incorporated in the samples have been given in a previous study.[24] The most stable structure is Bernal (AB) stacking of the h-BN and graphene sheets, like that of graphite, where the nitrogen atom is located above the center of a hexagon of graphene, and the impurity atom is stable when it is located on top of a nitrogen atom.[24] The supercell was an orthorhombic cell containing a graphene sheet and an h-BN sheet, having dimensions of 12.9×14.9×17.0 $Å^3$, with vacuum region of approximately 14-Å thickness. All the model systems were relaxed until the residual atomic forces were less than 0.02 eV·$Å^{-1}$. To describe the interaction between the electrons and ions, we used the generalized gradient approximation (GGA) with one of the functional forms proposed in Ref. 33 within the projector-augmented wave (PAW) method.[34] An energy cutoff of 400 eV and a Γ-centered 3×3×1 k-point sampling were employed to calculate the total energy and to obtain fully relaxed geometries. In the calculations, corrections were made for the vdW interaction between the metal impurity and the two sheets, using Grimme's DFT+D2 method.[35]

III. RESULTS AND DISCUSSION

A. Atomic force microscopy

We first consider the simulated AFM images of the free-standing graphene and h-BN monolayers. Figure 1 shows the AFM images obtained from the calculations for the separate graphene and h-BN monolayers, at two different tip heights (h) of 2 and 4 Å. It has been shown that h can alter the AFM image contrast significantly for some systems.[25, 36] Using the two values stated above, we also observe dramatic changes in contrast for both the graphene and h-BN cases. When the tip was close to the graphene surface ($h = 2$ Å), all the C sites appeared brighter in the resulting image [Fig. 1(a)]. The brighter spots correspond to the higher-frequency changes. However, contrast inversion occurred when the tip was simulated further from the surface ($h = 4$ Å), as shown in Fig. 1(b). In that case, brighter spots appeared at the graphene hollow sites. Since the force and frequency shift in our AFM simulation method solely depend on variations of the electrostatic potential of the substrate, the contrast inversion is related to the variation rate of the electrostatic potential. On top of the C atom, the electrostatic potential varies more rapidly compared to the hollow regions at a small tip-sample distances, which leads the result of higher brightness on C atom sites for a short separation from the surface. At a larger tip-sample distance, due to the constructive sum of π-bonding states originating from the hybridization of p_z orbitals of six C atoms, the electron density around the hollow site is higher than the C atom site. Consequently, brighter spots are visible at the hollow sites at the larger tip-sample distance (4 Å). According to our electronic charge densities integrated between -20 eV and 0 eV (the Fermi energy), the general features that the simulated STM images show are very similar to the AFM images for the two tip-sample distances (2 and 4 Å). For the monolayer h-BN, no such inversion occurred, *i.e.*, the hollow sites were never imaged as being brighter than the B or N atom sites. At $h = 2$ Å, only the B sites were apparent in the AFM image [Fig. 1(c)]. For $h = 4$ Å, in contrast, the N atom sites were represented by bright spots, which were slightly smaller and darker than those of the B atom sites [Fig. 1(d)]. We expect the B atom dominates the spectra over the distances within the simulation tip-surface distance range. At very small tip-sample distances (a few angstroms), a strong repulsive force occurs between the tip and substrate atoms, owing to the overlap of the electronic orbitals at atomic distances. Since N has a smaller atomic radius than B, a strong repulsive force is caused by the B atom with a larger radius; the empirical atomic radii of B and N are 0.85 and 0.65 Å, respectively. Thus, the B atoms are more visible than the N atoms at a smaller tip-sample distance (2 Å). However, for a larger tip-sample distance, the variation rates of the attractive electrostatic potential become similar for both B and N, and we observed bright spots on both atom sites at 4 Å in the AFM simulation result.

We next simulated AFM images of graphene/h-BN heterostructures with intercalated defects of Li, K, Cr, Mn, Co, and Cu. The fully optimized structures are shown in Figure 2. In our heterostructures, the h-BN sheet always exhibits greater deformation than the graphene sheet. The displacements of both the graphene and h-BN layers are listed in Table I. These values were calculated based on the vertical coordinate difference between the nearest and furthermost C and N atoms from the impurity atom. This difference can be interpreted as the difference in stiffness between the graphene and h-BN sheets, *i.e.*, the graphene sheet is stiffer than the h-BN sheet.[37] We find that intercalated K atom results in an especially strong structural deformation in the h-BN layer. Atomic radius of K is especially larger than those of the other impurity atoms (Li, Cr, Mn, Co, and Cu). When the impurity atom is encapsulated between graphene and h-BN layers (the interlayer distance of $\sim$ 3.3 Å), the K atom affects two layers with a stronger force than the other impurity atoms. Thus, the K atom deforms the graphene/h-BN heterostructure much more severely among the impurities that we chose.

Two different AFM images were produced for each structure, i.e., one for the graphene side and the other for the h-BN side. Here, h is set to 4 Å. Figure 3 shows the AFM images on the graphene side, which displays a dramatic difference in contrast with respect to the impurity atoms. The AFM images in Fig. 3 can be categorized into three groups: Group 1: images of the heterostructures containing Li, Co, and Cu; Group 2: those containing Cr and Mn; Group 3: those containing K. Such dramatic differences in images are related to the deformation of the graphene sheet by the incorporated metal atom. In Group 1, the average displacement of the nearest six C atoms from the impurity atom is $\sim$ 0.07 Å in the normal direction relative to the graphene plane. For Group 2, the average positional changes of the nearest C atoms is $\sim$ 0.16 Å. The greatest structural deformation in the graphene layers is obtained for Group 3, as the average positional change of the nearest six C atoms is $\sim$ 0.4 Å.

Group 1 shows a hexagonal-like bright spot at the impurity site in the supercell. On the other hand, Group 2 shows a circle-like bright spot around the impurity site, which can be attributed to the second nearest C atoms from the intercalated atom. Unlike Group 1, the contributions from the six nearest C atoms are less distinctive in Group 2 AFM images. A clear graphene structure is also shown in the group 2 AFM images, outside the circle-like bright spot. The K intercalated structure (Group 3) exhibits the most distinctive AFM image among the six structures, as a darker spot at the impurity site is observed. This contrast conversion implies that a smaller frequency shift occurs at the K atom site compared to the graphene region with no impurity. We also observe that the C-C bonds appear as bright lines in Groups 2 and 3.

Figure 4 shows the force profiles calculated using Eq. 1. A line is also shown in Fig. 4(a) and (b), which indicates a relationship between the simulated AFM images and the forces. Group 1, for which only a single large, bright spot is apparent around the impurity atom, exhibits a relatively large force at the impurity site, compared to groups 2 and 3. The smaller forces for groups 2 and 3 at the intercalated atom causes the C-C bonds to appear as bright lines in the corresponding AFM image, as the force from each C-C bond is relatively small.

Figure 5 shows the AFM images created on the h-BN sides for $h = 4$ Å. As shown in Fig. 2 and Table I, the h-BN sheet deforms greater than graphene for all intercalated atoms. Further, compared to the graphene AFM images [Fig. 3], there are less pronounced differences between the AFM images featuring the various impurities on the h-BN side. For $h = 4$ Å, all the AFM images show triangular-like bright spots at the impurity sites, apart from the K-incorporated structure which has a darker spot at the impurity site. This result is similar to the previous graphene 4-Å images, where only the K-atom case exhibits contrast inversion. The bright or dark spots are also related to the force profile and atomic displacement, as illustrated in the case of the graphene AFM images. On the h-BN side, the structure can be classified into two groups according to Table I: the structures with lesser (Li, Cr, Mn, Co, and Cu) and greater deformation (K). The structures with lesser and greater deformation exhibit smaller and larger forces, respectively. This trend is opposite to the graphene force-structural deformation relationship. In the force plot in Fig. 4(d), the force peak appears at the B site, which is not the nearest atom relative to the impurity. On the graphene side, however, the highest peak is at the impurity site (the hollow site of the graphene sheet). As the highest force peak is positioned on the B atom site, the h-BN AFM images have triangular features that are distinguishable from the graphene AFM images. The impurity metal atom is vertically located on top of an N atom in the h-BN layer, and the nearest neighbors of the N atom are three B atoms. For the K-intercalated structure, the darker color on the impurity atom site is related to our previous findings from Fig. 1(c) and (d). As the intercalated K atom causes greater protrusion of the h-BN layer, the N atom, which is located on top of the K atom, is closer to the AFM tip. Owing to the smaller tip-surface distance, the B atom sites are bright, however, this is not the case for the N atom sites. In h-BN AFM images, particular B/N sites or B-N bonds for the B and N atoms are not observed, when they are not located in the nearest neighbor site relative to the intercalated atoms.

B. Scanning tunneling microscopy

We obtained simulated STM images using Tersoff–Hamann theory and demonstrate that the single impurity atom between the graphene and h-BN sheets is detectable. Figure 6 shows the simulated constant-height mode STM images for $h = 2$ Å on the graphene side for the bias voltages of -2 and $+2$ V. In particular, the STM image of the negative bias of -2 V clearly exhibits three different types of STM patterns on the graphene side, which can again be classified into the same Groups 1 – 3 as previously outlined for our AFM images, which have hexagonal, circular, and wide bright spot patterns around the impurity atom, respectively. Although Co and Cu are both classed as Group 1, the Co atom exhibits stronger d orbital characteristics than the Cu atom. As explained in the discussion of the AFM simulation results, this result is due to the deformation of the graphene and h-BN layers by the intercalated metal atom. On the other hand, those of the positive bias of $+2$ V show two different types of patterns. For Li, Co, and Cu dopants, the STM images have darker spots at the the metal impurity sites. In contrast, the images for K, Cr, and Mn impurities show brighter spots at the the metal impurity sites.

Figure 7(a) shows that the Fermi level (E_F) is practically identical to the Dirac point of the graphene monolayer in the absence of an impurity metal atom, as only a weak van der Waals interaction appears between the graphene and h-BN sheets. Nevertheless, small orbital hybridization occurs between the graphene and h-BN layers, and the h-BN monolayer has a small density of states (DOS) between -1.5 and -1.0 eV.[24] Li, K, and Cu do not induce atomic spin magnetic moments, whereas Cr, Mn, and Co atoms do. For the incorporated Li or K atom, E_F moves towards the conduction band of graphene by ~ 0.7 eV, as shown in Fig. 7(b) and (c), respectively. We find that the DOS originating from the s orbitals of the Li (K) atom occurs at approximately +3 eV inside the conduction band. This means that almost one electron of the alkali impurity atom is donated to the graphene and h-BN sheets. On the other hand, the $3d$ transition metal impurities (Cr, Mn, Co, or Cu) result in strong orbital hybridization with the two sheets, which modifies the electronic and magnetic properties of the graphene/metal atom/h-BN sandwich structure. The Cr atom has strong DOS peaks at -1.2 and -0.7 eV for the spin-up states. A large DOS peak in the Mn impurity case appears at $+0.5$ eV. For the Co atom, large peaks occurs at -0.5 eV and very close to E_F for the spin-down electron. The results are similar to those previously reported for Mn and Co adsorption on graphene.[42, 43] As the $3d$ orbitals of the Cu atom are fully filled, the projected DOS (PDOS) of the $3d$ states is not shown in the energy range of -2 to $+2$ eV.

We examined whether or not the STM could detect the atomic orbital wave functions of the metal positioned between graphene and h-BN sheets. In previous STM experiments on carbon nanopeapods consisting of carbon nanotubes (CNTs) encapsulating fullerenes, it was found that the inserted fullerenes were imaged as a result of changes in the local electronic structures of the tubes.[44, 45] For instance, the STM image on C_{60}@CNT shows a modulation of the DOS in the conduction band. Using a computational scanning-tunneling-spectroscopy (STS) simulation, Cho *et al.*[46] found fullerene-originating states occurred at the location of the metallofullerene molecule when Gd@C_{82} was encapsulated. The intercalation energies and atomic spin magnetic moments of Co and Mn are large, and so we focus on the STM simulation of the two impurities. Figure 8(a) shows the computationally simulated constant-height mode STS images obtained in this study, for $h = 2$ Å and for both the graphene and h-BN sides of the vertical heterostructures. The atomic DOS plot of the Co atom in the graphene/Co/h-BN heterostructure is also shown. This heterostructure was considered because the Co atom has the localized states very close to E_F as shown in Fig. 7(f). For the h-BN side, all the simulated STS images exhibit overall three-fold symmetry. The metal atom was positioned immediately above a single N atom in the h-BN sheet, and thus had three-fold symmetry with respect to the h-BN layer. On the other hand, we observed interesting features in the STS images for the graphene side. The STS image integrated between -1.0 and -0.9 eV was symmetrical about the vertical axis; this behavior was due to the Co $3d_{xz}$ orbital at -0.90 eV, as shown in the atomic DOS. In contrast, the image integrated between -0.9 and -0.8 eV was symmetrical about the horizontal axis; this behavior was due to the Co $3d_{yz}$ orbital at -0.81 eV. Mixing of $3d_{xy}$ and $3d_{x^2-y^2}$ occurred at -0.73 eV, causing a hexagonal STS image integrated between -0.8 and -0.7 eV. In addition, Co $3d_{z^2}$ at -0.53 eV gives rise to a bright circular STS image. Since the remaining part of the image is very dark, we conclude that the $3d_{z^2}$ orbital is more extended than $2p_z$ orbital. (We integrated the electronic density on a plane $\sim$ 3.5 Å from the center of the metal atom.)

The most interesting feature of the intercalated Co atom is the localized impurity states near E_F. In the case of the Co atom, the simulated STM images obtained at bias voltages of -0.1 and $+0.1$ V differ significantly. The inset of the DOS plot in Fig. 8 shows that the Co $3d_{yz}$ orbital is hybridized with the Co $3d_{xz}$ orbital between -0.02 and $+0.02$ eV. In particular, a peak of the Co $3d_{yz}$ orbital is dominant at -0.01 eV while that of the Co $3d_{xz}$ orbital is dominant at $+0.01$ eV. Consequently, the simulated STS image integrated between -0.1 and 0.0 eV has a four lobe with mirror symmetry about the horizontal axis (the x axis), while the image integrated between 0.0 and $+0.1$ eV possesses a six-lobe configuration with bilateral symmetry about the vertical axis (the y axis). As the large Coulomb repulsion between the localized $3d$ orbitals may be poorly represented by a conventional DFT functional, we also added a Hubbard U term to the DFT functional to assess this issue. As U increases, the occupied $3d$ states move deeper inside the valence band. For $U = 2$ eV, the Co $3d_{yz}$ and $3d_{xz}$ states are split because of the large Coulomb repulsion. However, a localized state originating from the Co atom still occurs at E_F. Thus, the Co-derived states at E_F may act as scatterers for electronic transport in the graphene sheet. However, if a molecule adsorbed on the graphene or h-BN sheet at a position very close to the Co atom accepts (donates) charge from (to) the Co atom, the Co-derived localized states become distant from E_F, thereby weakening the scattering effect.

As shown in Fig. 8(b), the occupied Mn $3d_{yz}$ and $3d_{xz}$ orbitals were hybridized at -0.5 eV. In the vicinity of E_F, the Mn $3d_{x^2-y^2}$ orbital occurred at -0.1 eV. An interesting feature is that the Mn $3d_{z^2}$ orbital is unfilled while the Co $3d_{z^2}$ orbital is filled. Therefore, the Mn impurity is distinguishable from the Co impurity, when the bias voltage is examined for the bright spot-shaped STS image originating from the $3d_{z^2}$ orbital.

IV. CONCLUSION

We investigated the structural and electronic characteristics of vertical heterostructures comprising graphene and h-BN layers with intercalated defects (metal impurity atoms), by simulating AFM and STM images based on pseudopotential-density functional theory with corrections for van der Waals forces. Our AFM simulations reveal that the degree of structural deformation of the graphene and h-BN sheets, which is related to the intercalated atom, is the main factor altering the contrast in the AFM images. Our STS simulations reveal that C $2p_z$–Co $3d_{yz}$ hybridization occurs at a bias voltage of -0.1 V, while C $2p_z$–Co $3d_{xz}$ hybridization occurs at a bias voltage of $+0.1$ V. We conclude that STM can detect the localized electronic states originating from the atomic orbitals of a metal atom located between graphene and h-BN layers. The simulations presented here also suggest that subatomic-resolution AFM and STM may constitute useful tools for the characterization of the intercalated impurity atoms in graphene/h-BN heterostructures. Although we considered only the lattice-matched graphene/h-BN heterostructure, lattice mismatch between graphene and h-BN occurs, and results in the moiré pattern, in experiments.[47, 48] If the impurity atom exists in a moiré structure, we could expect the AFM and STM images may be somewhat complicated. However, the interaction between graphene and h-BN generating the moiré pattern is weaker than the coupling between the intercalated metal atom and graphene (or h-BN) layer. Even for the lattice-mismatch case, the overall features of AFM and STM images near the impurity region are similar to the lattice-match case since the pattern of AFM and STM images highly depend on the surface deformation and/or strong electronic coupling of metal impurity to the sheet near the impurity site. Besides, since we focus on the coupling between the metal impurity and one of the two layers, particular STM patterns that the $3d$ transition metal impurities show appear even for the lattice-matched graphene/h-BN heterostructures.

ACKNOWLEDGMENTS

JL and GK acknowledge the support of the Basic Research program (Grant No. 2012-0001743) and the Priority Research Center Program (Grant No. 2012-0005859) of the Korean Government MEST. MK and JRC would like to acknowledge support from the Welch Foundation Grant F-1837 and from the Department of Energy for work on nanostructures from Grant DE-FG02-06ER46286. Our research used resources of the National Energy Research Scientific Computing Center, a DOE Office of Science User Facility supported by the Office of Science of the U.S. Department of Energy under Contract No. DE-AC02-05CH11231.

[1] A. K. Geim and I. V. Grigorieva, Nature (London) **499**, 419 (2013).

[2] L. Britnell, R. V. Gorbachev, R. Jalil, B. D. Belle, F. Schedin, A. Mishchenko, T. Georgiou, M. I. Katsnelson, L. Eaves, S. V. Morozov, N. M. R. Peres, J. Leist, A. K. Geim, K. S. Novoselov, and L. A. Ponomarenko, Science **335**, 947 (2012).

[3] T. Georgiou, R. Jalil, B. D. Belle, L. Britnell, R. V. Gorbachev, S. V. Morozov, Y.-J. Kim, A. Gholinia, S. J. Haigh, O. Makarovsky, L. Eaves, L. A. Ponomarenko, A. K. Geim, K. S. Novoselov, and A. Mishchenko, Nature Nanotechnol. **8**, 100 (2013).

[4] D. Pacile, J. C. Meyer, C. O. Girit, and A. Zettl, Appl. Phys. Lett. **92**, 133107 (2008).

[5] C. G. Lee, Q. Li, W. Kalb, X. Liu, H. Berger, R. W. Carpick, and J. Hone, Science **328**, 76 (2010).

[6] C. R. Dean, A. F. Young, I. Meric, C. Lee, L. Wang, S. Sorgenfrei, K. Watanabe, T. Taniguchi, P. Kim, K. L. Shepard, and J. Hone, Nat. Nanotechnol. **5**, 722 (2010).

[7] K. Watanabe, T. Taniguchi, and H. Kanda, Nat. Mater. **3**, 404 (2004).

[8] G. Giovannetti, P. A. Khomyakov, G. Brocks, P. J. Kelly, and J. Van den Brink, Phys. Rev. B **76**, 073103 (2007).

[9] Y. Shi, C. Hamsen, X. Jia, K. K. Kim, A. Reina, M. Hofmann, A. L. Hsu, K. Zhang, H. Li, Z.-Y. Juang, M. S. Dresselhaus, L.-J. Li, and J. Kong, Nano Letters **10**, 4134 (2010).

[10] K. K. Kim, A. Hsu, X. Jia, S. M. Kim, Y. Shi, M. Hofmann, D. Nezich, J. F. Rodriguez-Nieva, M. Dresselhaus, T. Palacios, and J. Kong, Nano Letters **12**, 161 (2012).

[11] M. Wang, S. K. Jang, W.-J. Jang, M. Kim, S.-Y. Park, S.-W. Kim, S.-J. Kahng, J.-Y. Choi, R. S. Ruoff, Y. J. Song, and S. Lee, Adv. Mater. **25**, 2746, (2013).

[12] R. Garcia and R. Perez, Surf. Sci. Rep. 47, 197 (2002).

[13] F. J. Giessibl, Rev. Mod. Phys. 75, 949 (2003).

[14] S. K. Hämäläinen, Z. Sun, M. P. Boneschanscher, A. Uppstu, M. Ijäs, A. Harju, D. Vanmaekelbergh, and P. Liljeroth, Phys. Rev. Lett. 107, 236803 (2011).

[15] J. Xue, J. Sanchez-Yamagishi, D. Bulmash, P. Jacquod, A. Deshpande, K. Watanabe, T. Taniguchi, P. Jarillo-Herrero, and B. J. LeRoy, Nat. Mater. 10, 282 (2011).

[16] R. Decker, Y. Wang, V. W. Brar, W. Regan, H.-Z. Tsai, Q. Wu, W. Gannett, A. Zettl, and M. F. Crommie, Nano Lett. 11, 2291 (2011).

[17] S. Morita, F. J. Giessibl, and R. Wiesendanger, Noncontact Atomic Force Microscopy, Springer, Berlin, Vol. 2 (2009).

[18] L. Gross, F. Mohn, N. Moll, P. Liljeroth, and G. Meyer, Science 325, 1110 (2009).

[19] J. Welker and F. J. Giessibl, Science 336, 444 (2012).

[20] L. Gross, F. Mohn, N. Moll, G. Meyer, R. Ebel, W. M. Abdel-Mageed, and M. Jaspars, Nat. Chem. 2, 821 (2010).

[21] N. Moll, L. Gross, F. Mohn, A. Curioni, and G. Meyer, New J. Phys. 12, 125020 (2010).

[22] Z. Sun, M. P. Boneschanscher, I. Swart, D. Vanmaekelbergh, and P. Liljeroth, Phys. Rev. Lett. 106, 046104 (2011).

[23] J. Tersoff and D. R. Hamann, Phys. Rev. B 31, 805 (1985).

[24] S. Park, C. Park, and G. Kim, J. Chem. Phys. 140, 134706 (2014).

[25] T.-L. Chan, C. Z. Wang, K. M. Ho, and J. R. Chelikowsky, Phys. Rev. Lett. 102, 176101 (2009).

[26] M. Kim and J. R. Chelikowsky, Appl. Surf. Sci. 303, 163 (2014).

[27] M. Kim and J. R. Chelikowsky, Appl. Phys. Lett. 107, 163109 (2015).

[28] Y. Zhou, Y. Saad, M.L. Tiago, and J. R. Chelikowsky, Phys. Rev. E 74, 066704 (2006).

[29] Y. Zhou, Y. Saad, M.L. Tiago, and J.R. Chelikowsky, J. Comp. Phys. 219, 172 (2006).

[30] N. Troullier and J. L. Martins, Phys. Rev. B 43, 1993 (1991).

[31] D. M. Ceperley and B. J. Alder, Phys. Rev. Lett. 45, 566 (1980).

[32] G. Kresse and J. Furthmüller, Phys. Rev. B **54**, 11169 (1996).

[33] J. P. Perdew, K. Burke, and M. Ernzerhof, Phys. Rev. Lett. **77**, 3865 (1996).

[34] G. Kresse and D. Joubert, Phys. Rev. B **59**, 1758 (1999).

[35] S. Grimme, J. Comp. Chem. **27**, 1787 (2006).

[36] M. P. Boneschanscher, J. van der Lit, Z. Sun, I. Swart, P. Liljeroth, and D. Vanmaekelbergh, ACS Nano 6, 10216 (2012).

[37] S. Zhao and J. Xue, J. Phys. D: Appl. Phys. 46, 135303 (2013).

[38] C. Barth, A. S. Foster, C. R. Henry, and A. L. Shluger. Adv. Mater. 23, 477 (2011).

[39] J. Zhang, P. Chen, B. Yuan, W. Ji, Z. Cheng, and X. Qiu. Science 342, 611 (2013).

[40] L. Gross, F. Mohn, N. Moll, B. Schuler, A. Criado, E. Guitian, D. Pena, A. Gourdon, and G. Meyer. Science 337, 1327 (2012).

[41] D. G. de Oteyza, P. Gorman, Y.-C. Chen, S. Wickenburg, A. Riss, D. J. Mowbray, G. Etkin, Z. Pedramrazi, H.-Z. Tsai, A. Rubio, M. F. Crommie, and F. R. Fischer. Science 340, 1434 (2013).

[42] Y. Mao, J. Yuan and J. Zhong, J. Phys.: Condens. Matter **20**, 115209 (2008).

[43] H. Johll and H. C. Kang, and E. S. Tok, Phys. Rev. B **79**, 245416 (2009).

[44] D. J. Hornbaker, S-J Kahng, S. Misra, B. W. Smith, A. T. Johnson, E. J. Mele, D. E. Luzzi, and A. Yazdani, Science **295**, 828 (2002).

[45] J. Lee, H. Kim, S.-J. Kahng, G. Kim, Y.-W. Son, J. Ihm, H. Kato, Z. W. Wang, T. Okazaki, H. Shinohara, and Y. Kuk, Nature (London) 415, 1005 (2002).

[46] Y. Cho, S. Han, G. Kim, H. Lee, and J. Ihm, Phys. Rev. Lett. **90**, 106402 (2003).

[47] C. R. Woods, L. Britnell, A. Eckmann, R. S. Ma, J. C. Lu, H. M. Guo, X. Lin, G. L. Yu, Y. Cao, R. V. Gorbachev, A. V. Kretinin, J. Park, L. A. Ponomarenko, M. I. Katsnelson, Y. N. Gornostyrev, K. Watanabe, T. Taniguchi, C. Casiraghi, H-J. Gao, A. K. Geim, and K. S. Novoselov, Nat. Phys. **10**, 451 (2014).

[48] J. Xue, J. Sanchez-Yamagishi, D. Bulmash, P. Jacquod, A. Deshpande, K. Watanabe, T. Taniguchi, P. Jarillo-Herrero, and B. J. LeRoy, Nat. Mater. **10**, 282 (2011).

TABLE I. Displacement of graphene and h-BN sheet with the existence of impurity atom

impurity atom	graphene	h-BN
Li	0.05	0.60
K	0.53	1.37
Cr	0.18	0.62
Mn	0.15	0.44
Co	0.05	0.42
Cu	0.06	0.54

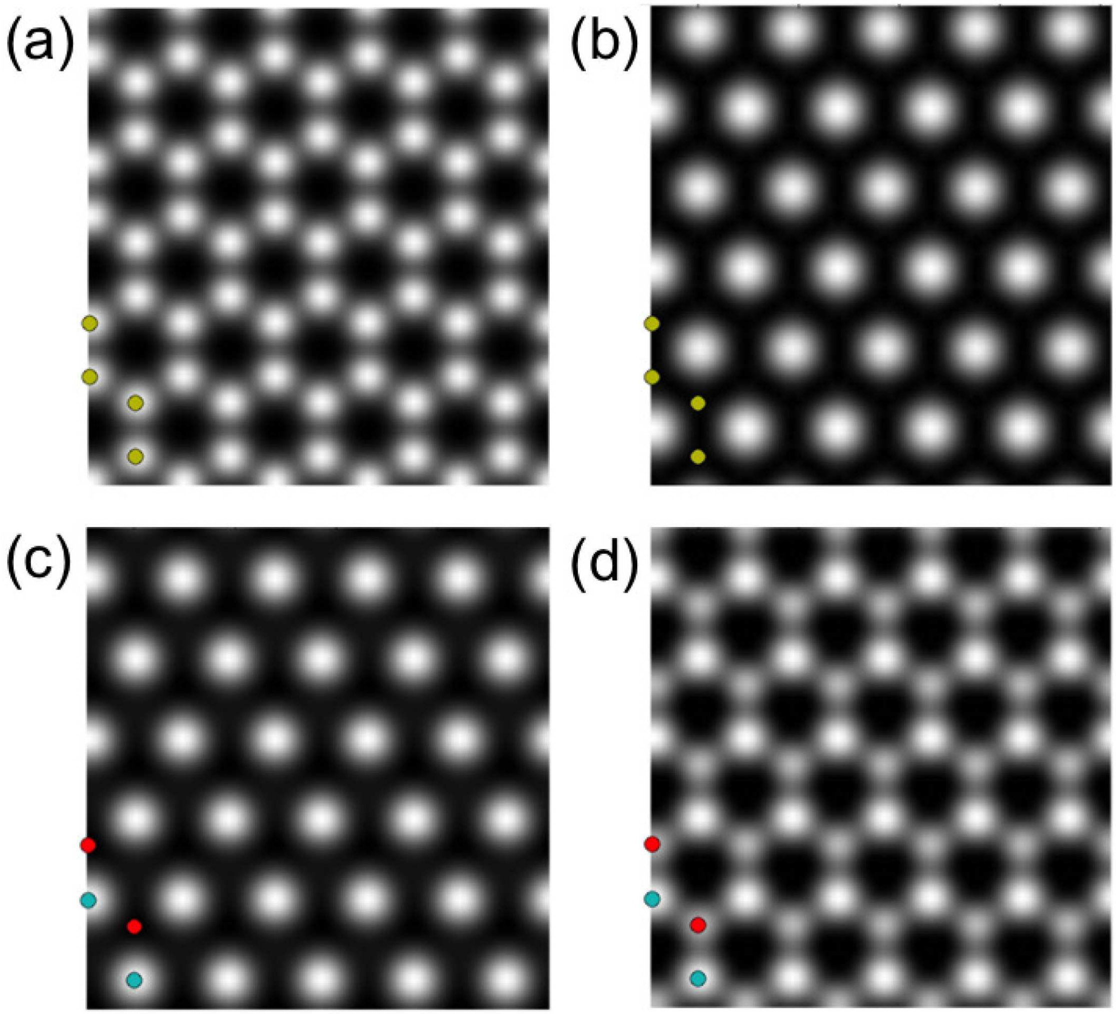

FIG. 1. Computationally Simulated AFM images for (a, b) graphene and (c, d) monolayer h-BN. Two different tip heights were employed: (a, c) 2 and (b, d) 4Å. The yellow, cyan, and red dots represent C, B, and N, respectively.

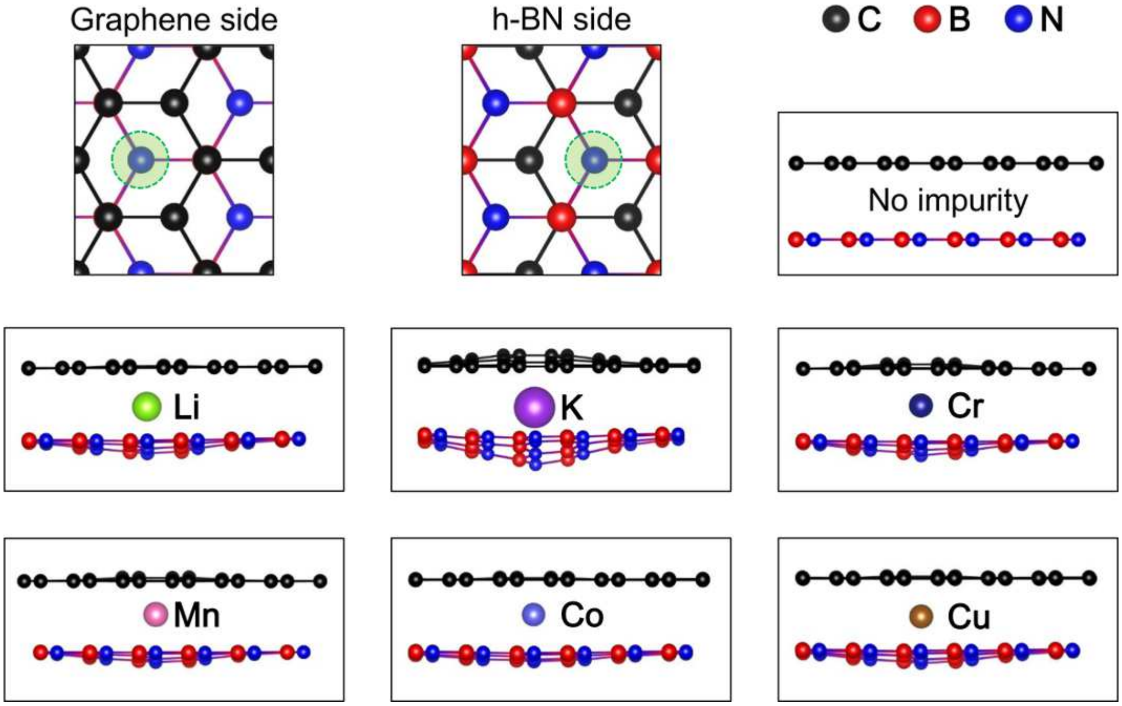

FIG. 2. Graphene/h-BN heterostructures with intercalated atoms. The upper and lower sheets are graphene (brown) and h-BN (green and grey), respectively.

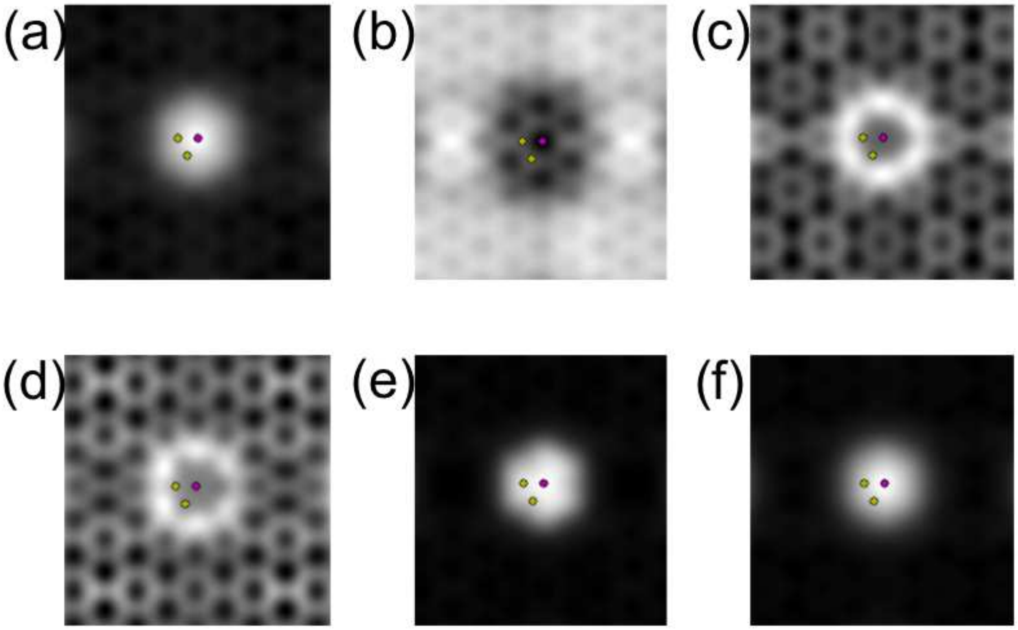

FIG. 3. Computationally simulated constant-height-mode AFM images for $h = 4$ Å on the graphene side. The purple dots indicate intercalated atoms, and the yellow dots denote two nearest C atoms. The intercalated atoms are: (a) Li, (b) K, (c) Cr, (d) Mn, (e) Co, and (f) Cu.

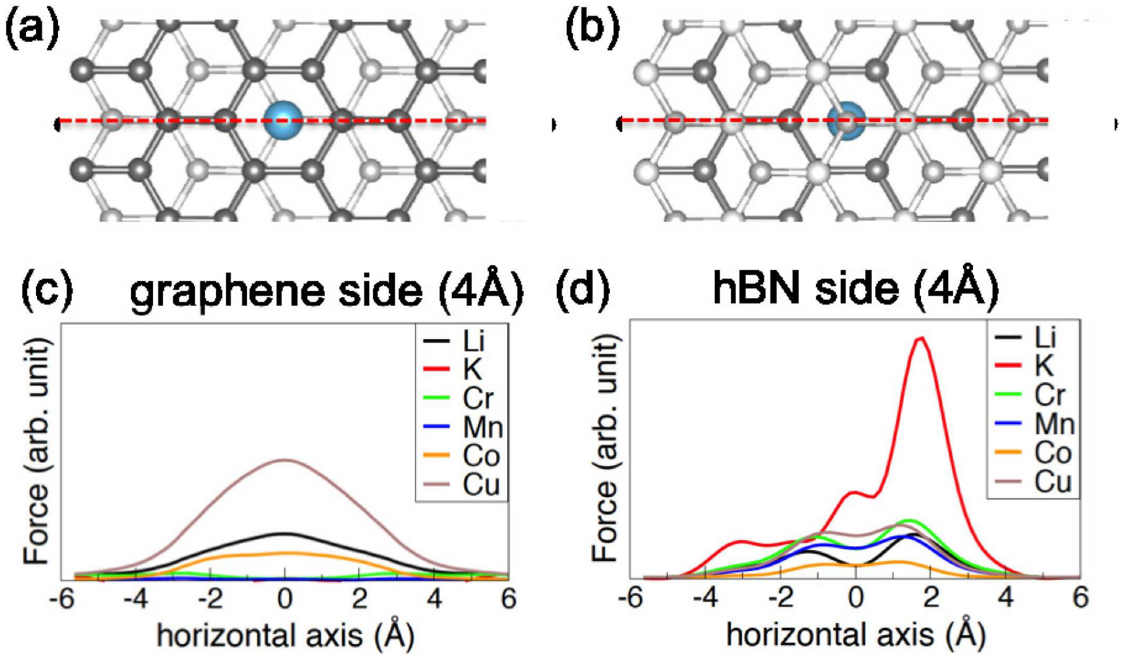

FIG. 4. Calculated force profiles for $h = 4$ Å on (a) graphene and (b) h-BN sides. The grey, silver, white and blue circles represent C, B, N, and the intercalated metal atom, respectively. The AFM tip moves along the red dotted line.

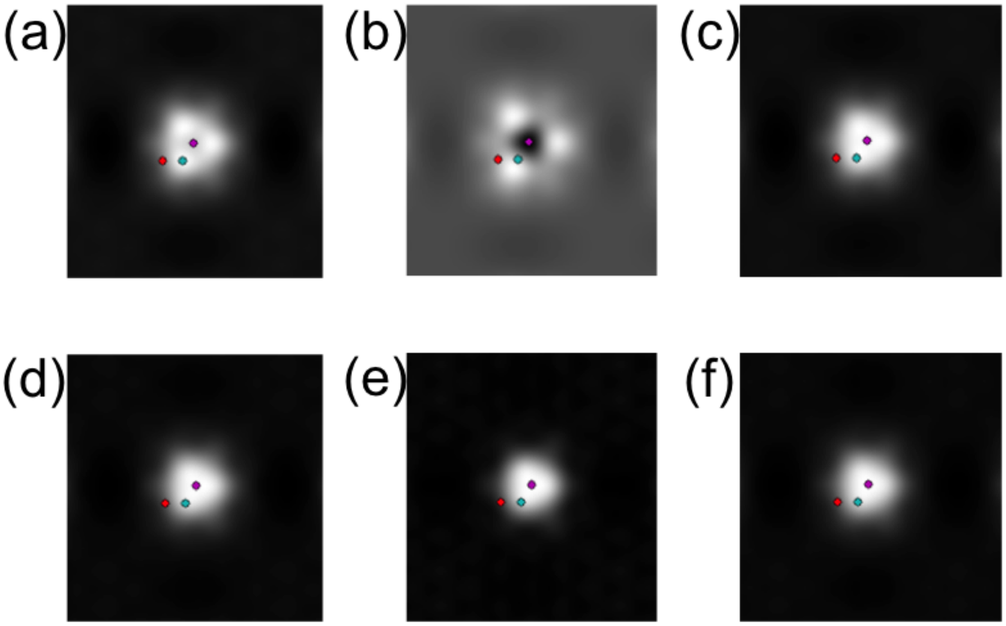

FIG. 5. Computationally simulated constant-height-mode AFM images for $h = 4$ Å on the h-BN side. The purple dots represent the intercalated metal atoms, while the cyan and red indicate B and N atoms, respectively. The intercalated atoms are: (a) Li, (b) K, (c) Cr, (d) Mn, (e) Co, and (f) Cu.

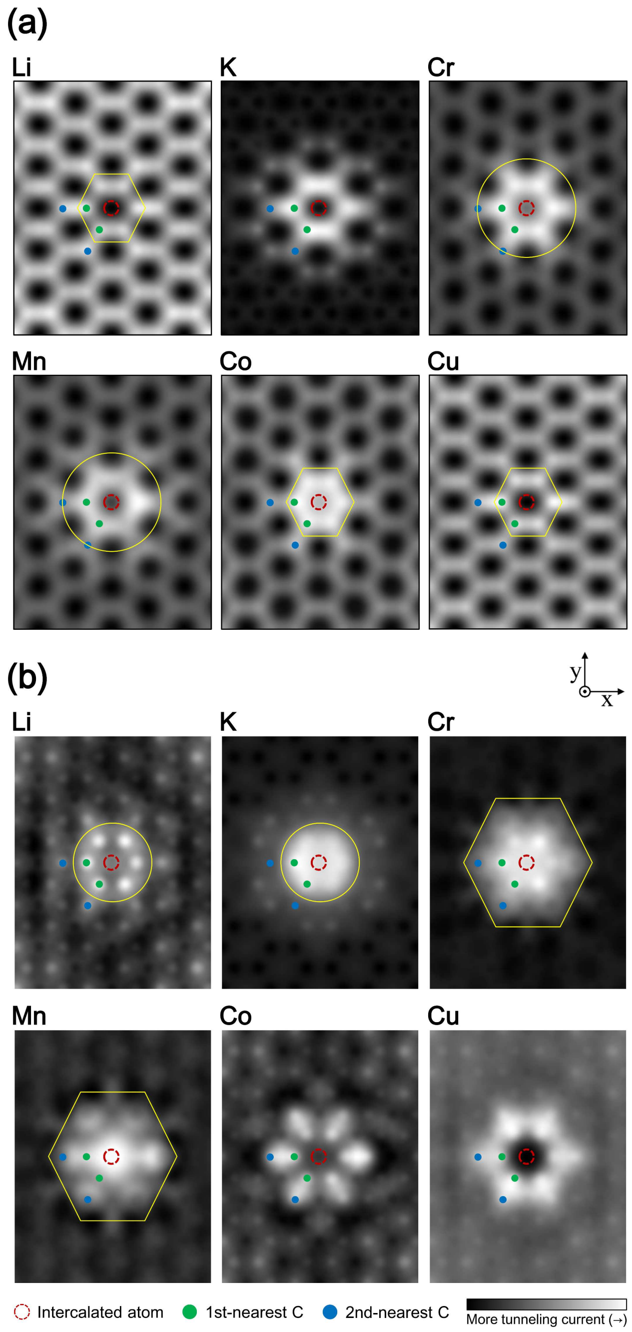

FIG. 6. Computationally simulated constant-height mode STM images for $h = 2$ Å on the graphene side for the bias voltages of (a) -2 and (b) $+2$ V. The red circles represent intercalated metal atoms, and the green dots indicate adjacent C atoms.

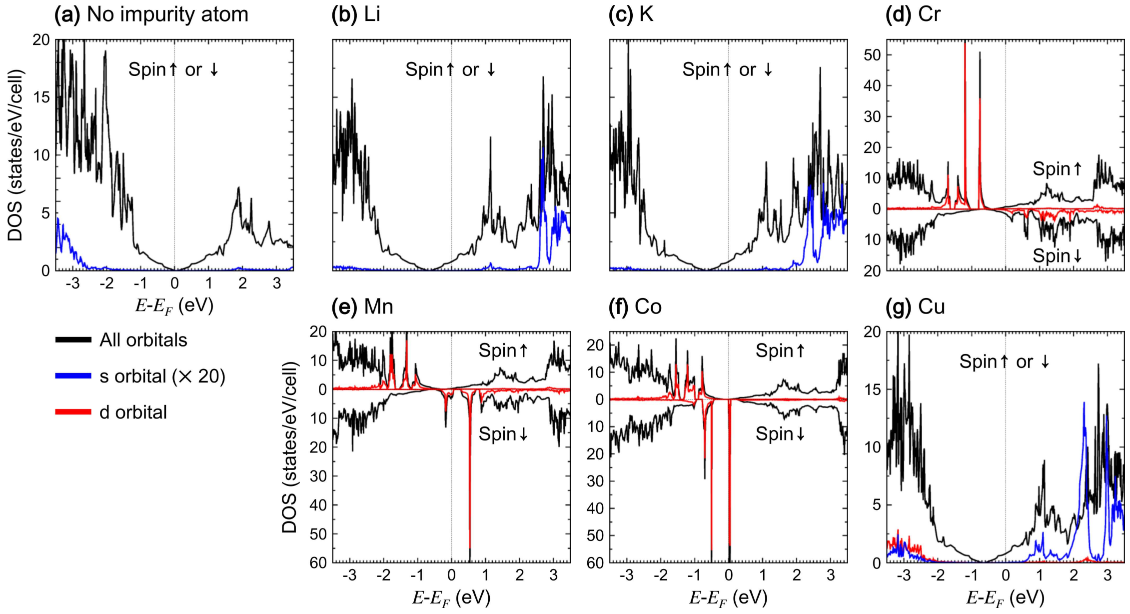

FIG. 7. Total and projected DOS plots of structures with (a) no impurity atom, and (b) Li, (c) K, (d) Cr, (e) Mn, (f) Co, and (g) Cu impurity atoms. For the *s* orbitals, the DOS is twenty times multiplied.

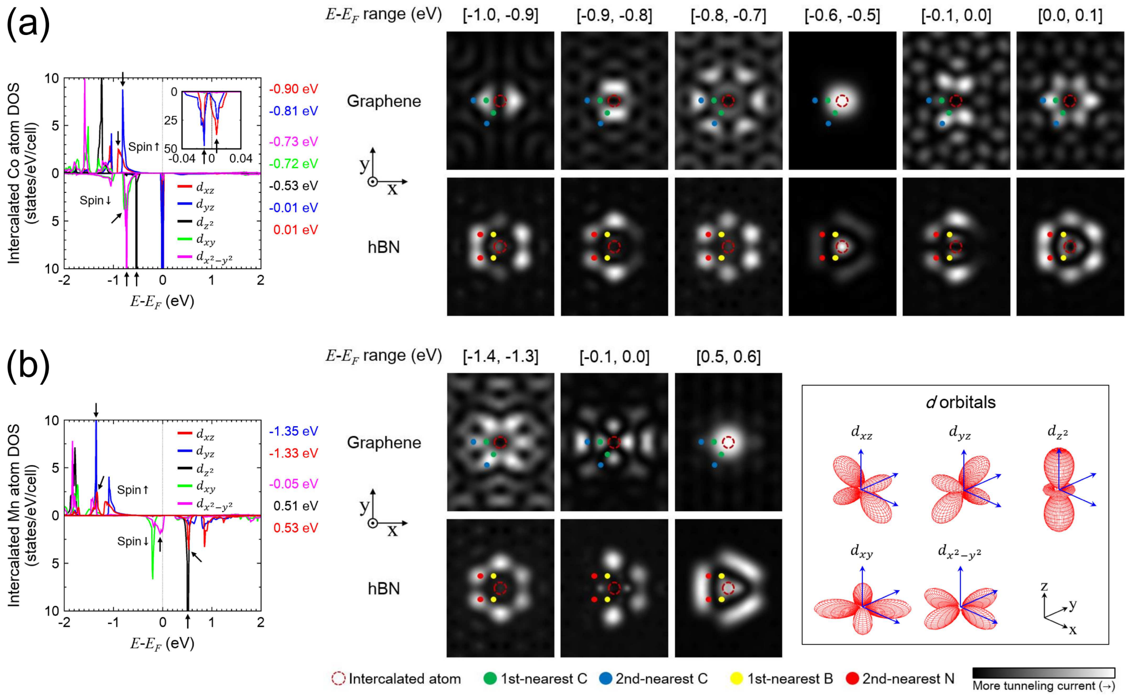

FIG. 8. Computationally simulated constant-height mode STS images for $h = 2$ Å on graphene and h-BN sides, along with atomic DOS of the metal atom in (a) the graphene/Co/h-BN heterostructure and (b) the graphene/Mn/h-BN heterostructure. The energy window for the integration is shown in parentheses above each image (units of eV). For the Co atom, the inset shows the atomic DOS near E_F. The DOS peaks indicated by arrows are chosen for the STS simulations at given energy windows.